Observation of the Griffiths phase in the ternary nitrides $Sn_{1-x}NFe_{3+x}$

Chaocheng Liu,[1] Xucai Kan,[1,*] Bosen Wang,[2,3,†] and Xiansong Liu [1,‡]

[1]*Engineering Technology Research Center of Magnetic Materials, School of Physics & Materials Science,*
Anhui University, Hefei 230601, China
[2]*Beijing National Laboratory for Condensed Matter Physics and Institute of Physics, Chinese Academy of Sciences,*
Beijing 100190, China
[3]*Songshan Lake Materials Laboratory, Dongguan, Guangdong 523808, China*

We report the synthesis and magnetic properties of ternary iron nitride compounds $Sn_{1-x}NFe_{3+x}$ ($0 \leqslant x \leqslant 0.4$). The magnetic frustration state is found in $SnNFe_3$, and the antiferromagnetic (AFM) exchange is dominant in $Sn_{0.95}NFe_{3.05}$ and $Sn_{0.9}NFe_{3.1}$, and then the ferromagnetic (FM) interaction occurs in $Sn_{1-x}NFe_{3+x}$ ($0.2 \leqslant x \leqslant 0.4$). Interestingly, the Griffiths phase is observed in $x = 0.1, 0.2$, caused by the FM coupling competing over the AFM one and forming the short-range FM cluster. At the same time, the competitions between the AFM and FM interactions lead to a spin-glass behavior, which is embodied most evidently in $Sn_{0.7}NFe_{3.3}$ and further confirmed by the corresponding characteristic fitting parameters ($\tau_0 = 8.89 \times 10^{-12}$ s, $T_0 = 25$ K, and $zv = 6.56$). In addition, density functional theory (DFT) calculations exhibit the magnetic ground states, magnetic moments contribution, and bonds nature of Sn-Fe and N-Fe. The results of DFT calculations disclose some detailed magnetic interactions, which are demonstrated to be an evidential response to the interesting magnetic behavior in $Sn_{1-x}NFe_{3+x}$ compounds.

I. INTRODUCTION

In 1969, Griffiths theoretically predicted a particular short-range ferromagnetic (FM) correlation in randomly diluted Ising ferromagnets, which was later called the Griffiths phase (GP) [1]. The Griffiths phase accounts for a magnetic system where a random distribution of the magnetic interaction is induced by disorder, which always exists in a Griffiths temperature scale T_G above the magnetic ordering temperature T_c [2]. In its simplest form, the original problem of GP is to consider the percolative nature of an Ising system, where the nearest neighbor (exchange) bonds are characterized by strength J with probability $p(0 \leqslant p \leqslant 1)$ [3]. Below the percolation threshold ($p < p_c$), an infinite percolating *backbone* cannot be formed, that is to say, the cooperative FM transition cannot occur as expected. However, for $p > p_c$, the FM phase is established at a temperature $T_c(p)$, which is lower than the critical temperature $T_G[T_c(p = 1) = T_G]$ (i.e., Griffiths temperature). In the temperature range of $T_c(p) < T < T_G$, the disordered system is between the conventional paramagnetic (PM) state and the ordering FM phase, and results in the appearance of GP [4]. The GP is closely related to the quenched disorder and competing interactions [5], which is always found in the diluted quasi-two-dimensional magnet [6], diluted magnetic semiconductor [7], Mn-based perovskite/double perovskite compound [8,9], rare earth intermetallic compound [10], etc. However, there are not many GP compounds in some of the antiferromagnetic (AFM) interaction systems, which exhibit negative PM Weiss temperature (θ), such as Ca_3CoMnO_6 [9] and $GdFe_{0.17}Sn_2$ [11]. Thus it will be of great significance to choose and investigate an appropriate GP compound with AFM interaction, especially for other possible materials.

Recently, antiperovskite structural nitrides ANM_3 ($A =$ Ga, Al, Sn, Zn, Cu, In, Ge, etc.; $M =$ Mn, Fe, Ni, Cr, etc.) have always attracted much attention because of the promising candidates for functionality and some interesting magnetic properties [12]. As a typical Fe-based antiperovskite nitride, $SnNFe_3$ is little known apart from the early studies focusing on synthesis processes and theoretical investigations. Especially, to date, and to the best of our knowledge, there are no reports in the literature about the GP in $SnNFe_3$. In our present work, we synthesized the Fe-based antiperovskite nitrides $Sn_{1-x}NFe_{3+x}$ ($0 \leqslant x \leqslant 0.4$) by a solid-state reaction method. And then, the comprehensive magnetic characterizations of $Sn_{1-x}NFe_{3+x}$ were performed systematically. Interestingly, with increasing x, an obvious evolution occurs from AFM interaction to FM interaction. A magnetic frustration (MF) state is found and investigated in $SnNFe_3$. In particular, the GP is found in $Sn_{1-x}NFe_{3+x}$ which emerges in $Sn_{0.9}NFe_{3.1}$, $Sn_{0.8}NFe_{3.2}$, and disappears with increasing x level to $Sn_{0.6}NFe_{3.4}$. Meanwhile, the spin glass (SG) behavior also appears in specific doping scale at lower temperature, and further analyses show that the competitions between the FM and AFM interactions should be responsible for the observed SG behavior in this system.

II. EXPERIMENTAL DETAILS

The polycrystalline $Sn_{1-x}NFe_{3+x}$ ($0 \leqslant x \leqslant 0.4$) series of compounds were synthesized by the solid-state reaction. The

---

*Corresponding author: kanxucai@ahu.edu.cn
†Corresponding author: bswang@issp.ac.cn
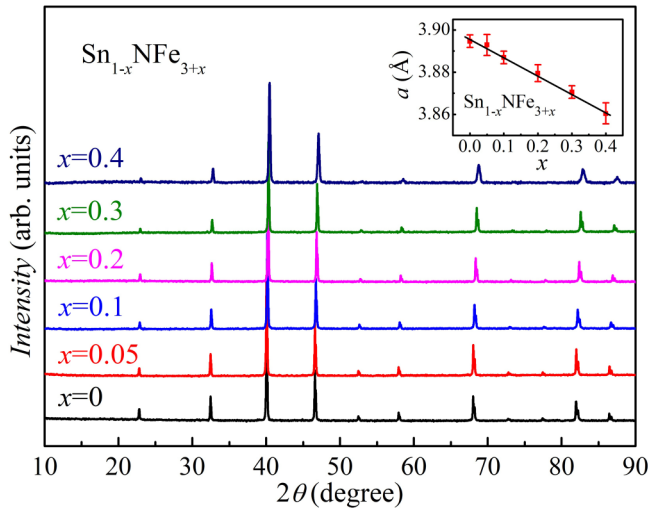‡Corresponding author: xiansongliu@ahu.edu.cn

FIG. 1. Room-temperature x-ray diffractions of $Sn_{1-x}NFe_{3+x}$ ($0 \leqslant x \leqslant 0.4$). The inset shows lattice parameter as a function of x.

starting materials of the powdered oxides SnO_2 (4N) and Fe (3N) were weighed according to the specific stoichiometric ratio, thoroughly ground, and then annealed at 923–973 K for 10 h in flowing NH_3 atmosphere (500 cc/min). After quenching to room temperature, the products were pulverized, mixed, pressed into pellets, and annealed again for 10 h in order to obtain the homogeneous samples. The structure and phase analyses were performed by x-ray diffractometer with Cu-$K\alpha$ radiation (Philips, $\lambda_{\alpha 1} = 1.5406$ Å, $\lambda_{\alpha 2} = 1.5443$ Å, and $K\alpha_1 : K\alpha_2 = 2 : 1$). Field emission scanning electron microscopy (FE-SEM) was F used to determine the morphology and element content. Magnetic measurements were performed on a superconducting quantum interference device magnetometer based on magnetic property measurement system
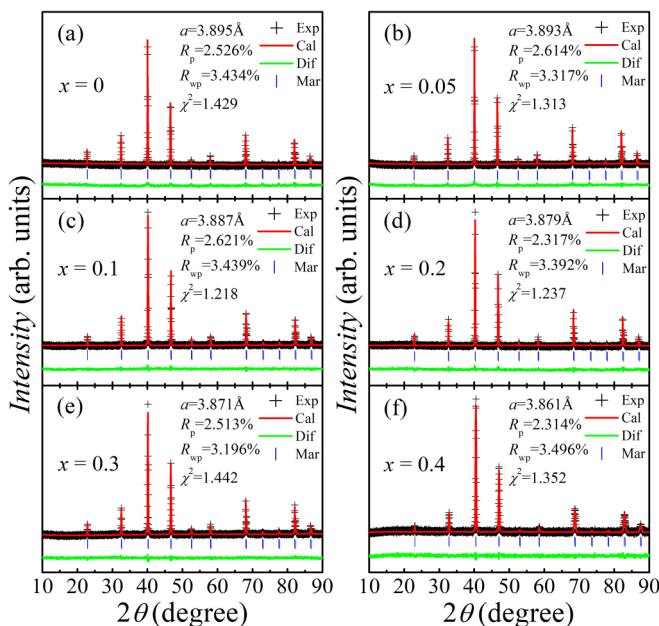

FIG. 2. The Rietveld refined powder XRD patterns at room temperature for $Sn_{1-x}NFe_{3+x}$ ($0 \leqslant x \leqslant 0.4$) compounds.
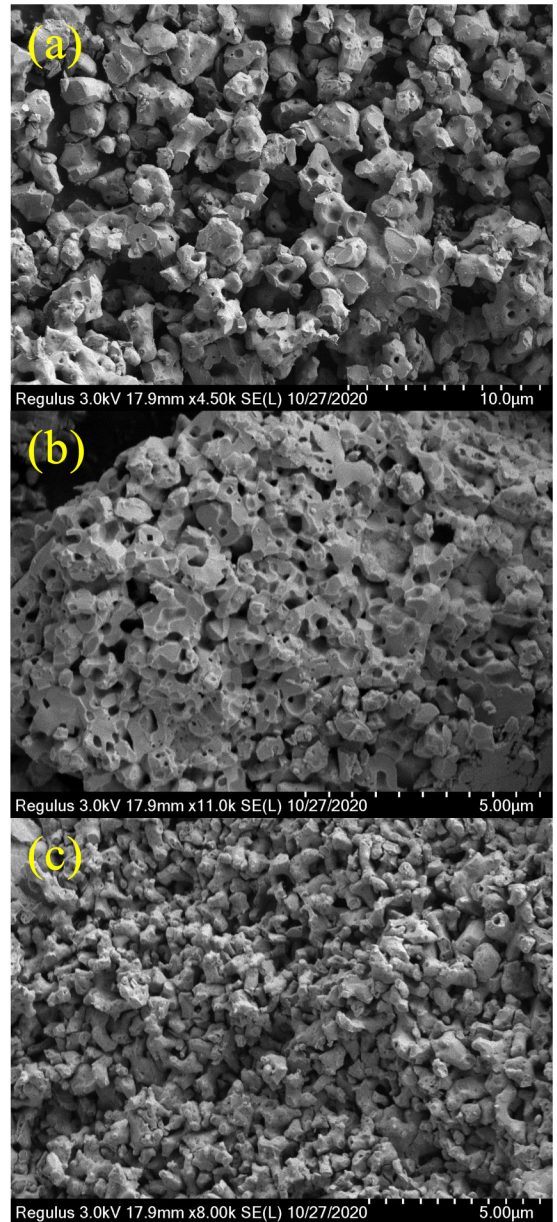

FIG. 3. The morphology of $Sn_{1-x}NFe_{3+x}$ ($0 \leqslant x \leqslant 0.4$) compounds with several representative doping concentration: (a) for $x = 0$; (b) for $x = 0.2$; (c) for $x = 0.4$.

(SQUID-MPMS 3) from Quantum Design, USA. The electron spin resonance (ESR) spectroscopy was determined by using a Bruker EMX plus 10/12 (equipped with Oxford ESR910 liquid helium cryostat) at X band $v = 9.4$ GHz. The theoretical calculations of the structure and magnetic properties were carried out by using the CASTEP (Cambridge Serial Total Energy Package) code [13]. The density of state (DOS) and electronic structure were calculated and analyzed from density functional theory (DFT) [14]. The generalized gradient approximation (GGA) with the Perdew, Burke, and Ernzerhof (PBE) functional was used to estimate the exchange correlation [15]. The $8 \times 8 \times 8$ Monkhorst-Pack k-point grid for one supercell containing eight formula units was used for Brillouin-zone integration superimposed by the energy cutoff of 600 eV.
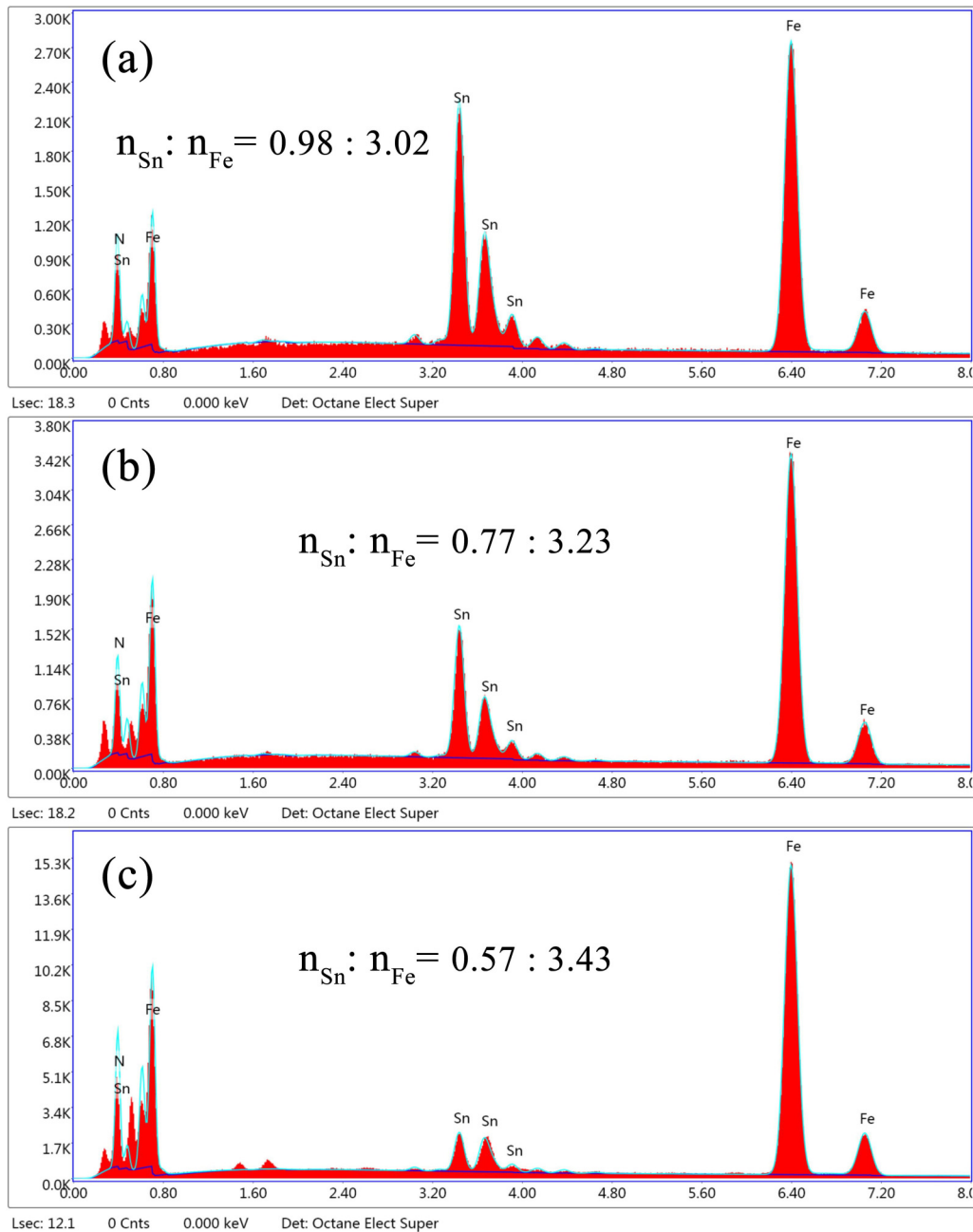
FIG. 4. Energy dispersive x-ray (EDX) spectra of $Sn_{1-x}NFe_{3+x}$ ($0 \leqslant x \leqslant 0.4$) compounds with some specific doping concentration: (a) for $x = 0$; (b) for $x = 0.2$; (c) for $x = 0.4$.

III. RESULTS AND DISCUSSION

Figure 1 presents the powder XRD patterns of $Sn_{1-x}NFe_{3+x}$ ($0 \leqslant x \leqslant 0.4$) at room temperature. All the samples are single phase with a standard cubic antiperovskite structure (space group: $Pm3m$). The evolution of lattice parameters is refined by using the standard Rietveld technique and displayed in the inset of Fig. 1, where the radius of variants linearly decreases as x increases. The lattice parameter a presents linear behavior as a function of the actual doping level x, suggesting that the actual doping level of Fe may be close to the nominal one. To better elaborate the phase of our samples, we perform the Rietveld

refinement of room-temperature powder XRD patterns of $Sn_{1-x}NFe_{3+x}$ ($0 \leqslant x \leqslant 0.4$) compounds as shown in Fig. 2. All the diffraction patterns can be well fitted by a cubic symmetry with reliable fitting parameters and no secondary phase is detected, indicating the prepared samples are fairly good in quality. The refined lattice parameter a is around 3.895 Å for $SnNFe_3$, which also coincides well with other similar results [16].

Since the lattice parameters evolve with different substituting x, it is necessary to know the corresponding changes of the crystallographic information for different compounds. Figure 3 shows the morphology of $Sn_{1-x}NFe_{3+x}$ ($0 \leqslant x \leqslant$
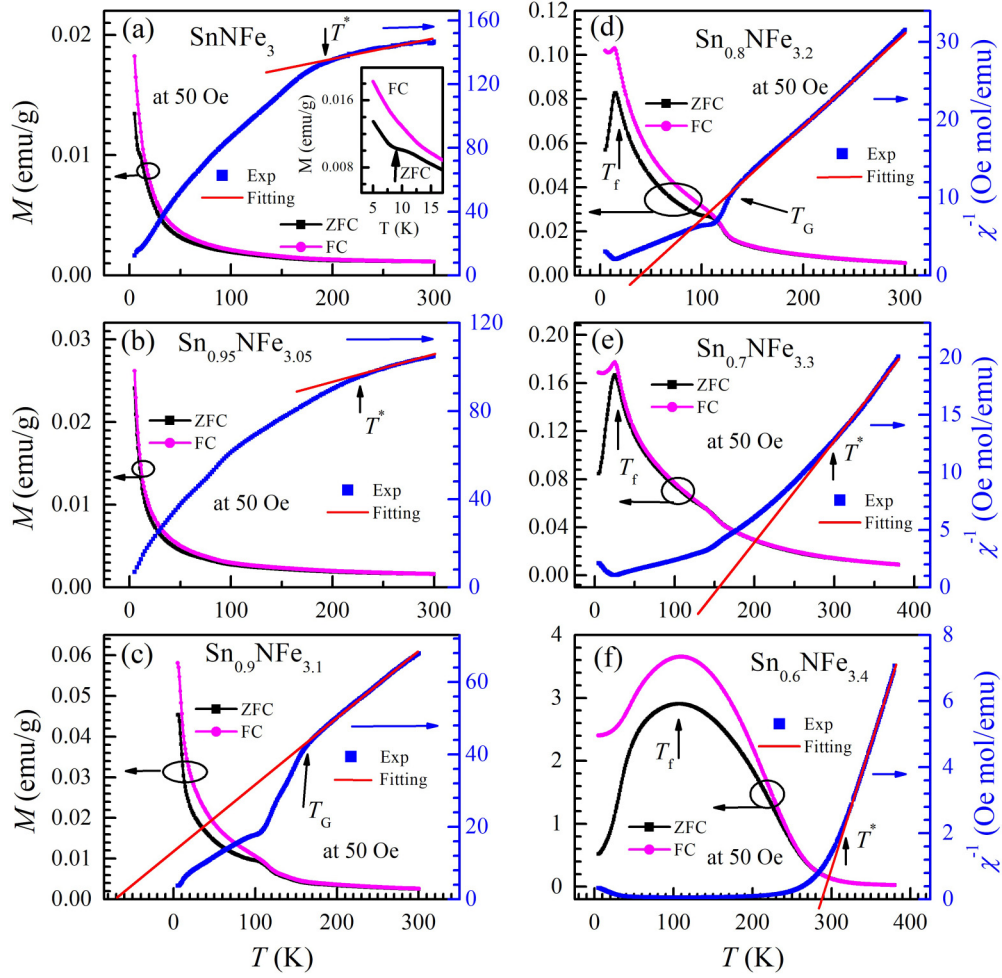
FIG. 5. The temperature dependent magnetization $M(T)$ and the inverse susceptibility $\chi^{-1}(T)$ curves of FC for $Sn_{1-x}NFe_{3+x}$ ($0 \leqslant x \leqslant 0.4$): (a) for $x = 0$. The inset shows the enlarged $M(T)$ patterns from 5 to 16 K; (b) for $x = 0.05$; (c) for $x = 0.1$; (d) for $x = 0.2$; (e) for $x = 0.3$; (f) for $x = 0.4$.

0.4) compounds with some representative substituting concentration. Specifically, Figs. 3(a)–3(c) refer to the doping concentration $x = 0$, 0.2, and 0.4 respectively. One can see that a quasicube shape is maintained at all given dopant levels. Considering the nonstandard cube morphology, a reasonable fact should be accepted that may be caused by grinding of powder samples. For the grain size, the average particle size of the compounds exhibits a slight decreasing trend as observed from the SEM image with specific marking scale, which is well compatible with the theoretical results of x-ray diffraction (XRD) analysis. Besides, the specific element composition and content are also performed and given in Fig. 4. The obtained atomic percentage is quite close to the theoretical one, suggesting the reliability of the experiments as well as the high quality of the prepared samples.

The left coordinates of Figs. 5(a)–5(f) show the temperature dependent magnetization $M(T)$ curves for $Sn_{1-x}NFe_{3+x}$ ($0 \leqslant x \leqslant 0.4$) at 50 Oe under zero-field cooled (ZFC) and field cooling (FC) processes. For $SnNFe_3$ [as shown in Fig. 5(a)], a shoulderlike platform is found in ZFC process, but no signs in the FC process [see inset of Fig. 5(a)]. A similar behavior was also found in $GaCCo_3$ [17], which is

attributed to the strong magnetic frustration. With increasing x to $x = 0.1$ and 0.2, as shown in Figs. 5(c) and 5(d), an unknown phase transition appears around 160 and 140 K, respectively. Meanwhile, for samples $x = 0.2$ to 0.4 [see Figs. 5(d)–5(f)], a weak irreversibility appears between the ZFC and FC curves at an irreversibility temperature T_{irr} (defined by the temperature where $M_{ZFC} = M_{FC}$) as well as a sharp cusp in the ZFC curve around T_f (defined by the maximum value of magnetization after the ZFC process), which are the typical fingerprints of the SG transition [18]. In order to further investigate the magnetic properties of $Sn_{1-x}NFe_{3+x}$ ($0 \leqslant x \leqslant 0.4$), the inverse susceptibility $\chi^{-1}(T)$ under the FC process is performed in the right coordinate of Fig. 5. Here, we define a temperature T^* as the characteristic temperature. Above T^*, the inverse susceptibility is linear temperature dependence. To get more information about the magnetism of $Sn_{1-x}NFe_{3+x}$, we make a well fitted $\chi^{-1}(T)$ curve by using the Curie-Weiss law [19]: $\chi^{-1}(T) = (T - \theta)/C$, where C stands for the Curie constant and θ is the Weiss temperature. As a result, the values of the parameters are obtained and listed in Table I. In addition, Table I also gives the effective PM moment per Fe atom, p_{eff}, estimated from the relationship [20]: $p_{eff} = 2.83(C_m/\eta)^{0.5}\mu_B$, where η is the number of magnetic

TABLE I. The obtained parameters (Curie constant C, Weiss temperature θ, and effective PM moment per Fe atom) for $Sn_{1-x}NFe_{3+x}$ samples.

x	0	0.05	0.1	0.2	0.3	0.4
C (emu K mol^{-1})	7.01	3.64	5.47	8.42	10.93	13.43
θ (K)	−747	−129	−74	37	163	287
p_{eff}/Fe(μ_B)	4.33	3.09	3.76	4.59	5.13	5.62

atoms in a unit cell and is equal to $3 + x$ in the present case.

To further verify the possible existence of the SG behavior, we perform detailed magnetic susceptibility measurements and characterizations for a more representative sample $Sn_{0.7}NFe_{3.3}$. As presented in Fig. 6(a), with increasing the external magnetic field H, both the T_f and T_{irr} shift to lower temperature, indicating that the frozen SG state is gradually destroyed under larger H [21]. In addition, the field dependence of T_f can be well described by the $H^{2/3}$ law [see the inset of Fig. 6(a)], which has been discovered in many SG systems such as SnCFe$_3$ [22] and GaNMn$_3$ [23]. To characterize the dynamic process of the SG phase in $Sn_{0.7}NFe_{3.3}$, the frequency dependence of ac susceptibility $\chi'(T)$ was measured and shown in Fig. 6(b). The $\chi'(T)$ exhibits strongly frequency-dependent peaks, that is, the peaks shifting to the high temperature region along with increasing frequency f. The relative variation of T_f is defined by $\delta T_f = \Delta T_f/[T_f \Delta \log_{10}(f)] \sim 0.0138$, a typical value for the canonical SG state (0.0045–0.08). At the same time, this value is close to those of SG systems with antiperovskite structure, such as GaNMn$_3$ ($\delta T_f = 0.037$) [23], SnCFe$_3$ ($\delta T_f = 0.0165$) [22], and PdNCr$_3$ ($\delta T_f = 0.0156$) [24], indicating a typical SG system for $Sn_{0.7}NFe_{3.3}$. Generally, in the SG system, the relaxation time is described by a power law [12]:

$$\tau = \tau_0[T_f(f)/T_0 - 1]^{-zv}, T_f > T_0, \qquad (2)$$

where T_0 is the freezing temperature, τ_0 is the characteristic flipping time, τ is the relaxation time [$\tau = 1/(2\pi f)$], and zv is the dynamical critical exponent. All the parameters ($T_0 = 25$ K, $zv = 6.56$, and $\tau_0 = 8.89 \times 10^{-12}$ s) are obtained by fitting the power law as displayed in the inset of Fig. 6(b), indicating a conventional SG [25]. Meanwhile, isothermal remanent magnetizations $M_{IRM}(t)$ were measured at different magnetic fields under the ZFC process and shown in Fig. 6(c). $M_{IRM}(t)$ decays so slowly that the magnetization value is nonzero even after several hours of decay, which is also an obvious fingerprint of SG behavior. The obtained experimental data of $M_{IRM}(t)$ can be fitted according to the formula [26] $M_{IRM}(t) = M_0 - \alpha \ln(t)$. The fitting parameters M_0 and α, plotted in the set of Fig. 6(c), increase with H up to 1000 Oe, and then reach the unsaturated point. These results confirm that the SG state in the present compound is similar to several other different SG states [22–24].

Besides, regarding the possible existence of GP, in Fig. 7, we show the inverse susceptibility data under different fields H for samples with $x = 0.1$ and 0.2. One can see that, on cooling, all the H/M curves exhibit a linear thermal dependence above T_G, indicating a Curie-Weiss behavior. For sample $x =$
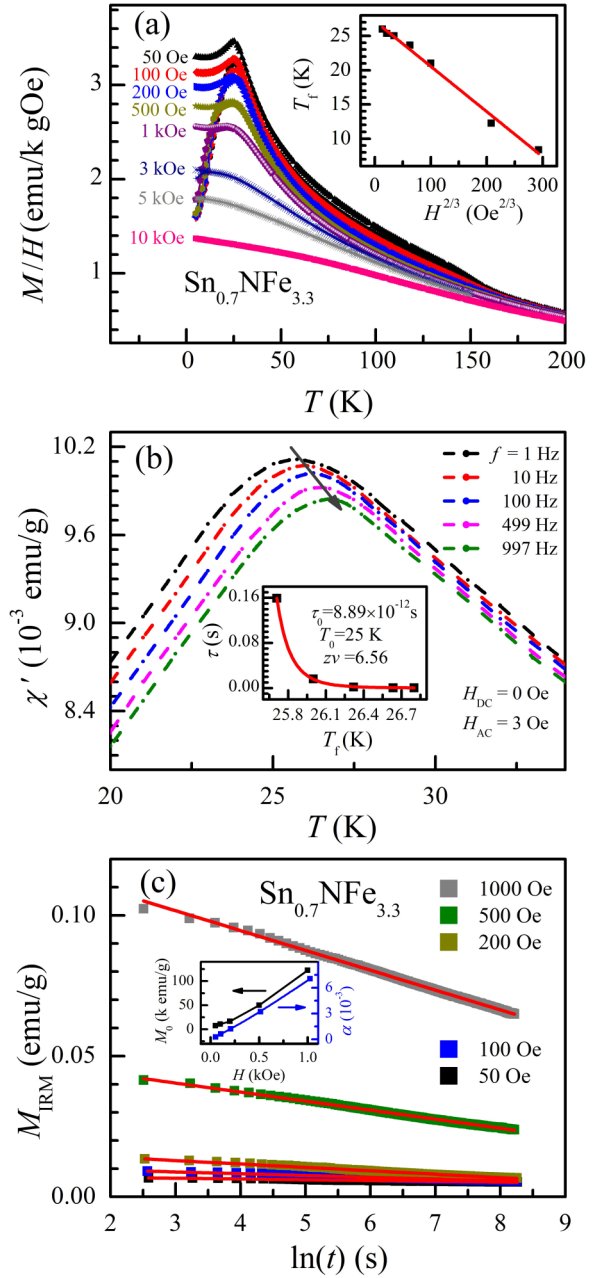

FIG. 6. (a) $M(T)$ curves under ZFC/FC processes at different H for $Sn_{0.7}NFe_{3.3}$. The inset displays T_f as a function of $H^{2/3}$. (b) Real components of ac susceptibility $\chi'_{AC}(T)$ at several fixed frequencies. The inset presents the best fit by a power law. (c) M_{IRM} vs $\ln(t)$ at different H and the solid lines are fitted by $M_{IRM}(t) = M_0 - \alpha\ln(t)$. The inset shows fitting parameters M_0 and α as a function of H.

0.1, as shown in Fig. 7(a), the fitted Weiss temperature θ is -74 K, indicating a strong AFM coupling. While with increasing Fe content to $x = 0.2$ [see Fig. 7(b)], the value of θ has changed into the positive one, that is 37 K, suggesting that FM interaction dominates [19]. Below T_G, all curves more or less have a downturn phenomenon, and as the magnetic field decrease, this downturn phenomenon becomes more and more apparent. In small magnetic field, a clear deviation from Curie-Weiss behavior is observed below T_G, while the FM component is hidden in the PM contribution and a Curie-
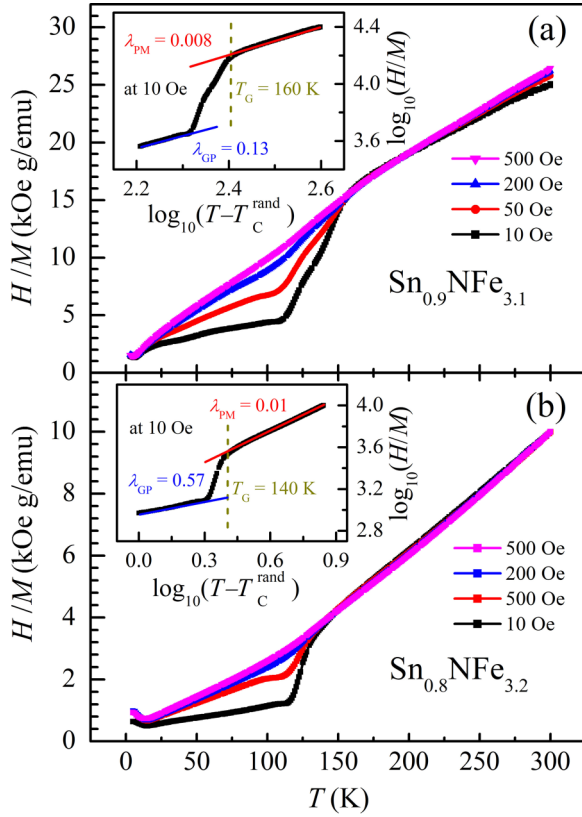
FIG. 7. $H/M-T$ curves under different H. The inset displays $\ln(H/M)$ as a function of $\log_{10}(T - T_C^{rand})$: (a) for $x = 0.1$; (b) for $x = 0.2$.

FIG. 8. The derivative ESR spectra (dP/dH) for $Sn_{1-x}NFe_{3+x}$ ($x = 0.1, 0.2$): (a) for $x = 0.1$ under the temperature from 2 to 190 K; (b) for $x = 0.2$ over the temperature range of 2 to 180 K.

Weiss law is found throughout the PM regime in a large applied field. Obviously, this downturn phenomenon of the H/M curves is a typical fingerprint of the GP, which is also observed in variety of other systems [27,28]. In order to confirm the GP of sample $x = 0.1, 0.2$, we analyze the magnetic susceptibility exponent equation [9], $H/M = (T/T_c^{rand} - 1)^{1-\lambda}$, where $0 \leqslant \lambda \leqslant 1$, as shown in the inset of Fig. 7. In the equation, T_c^{rand} (namely, the critical temperature for a random FM cluster) can be set as θ, T_N (Néel temperature), T_c, or a value above T_c [29]. Regardless of the value of T_c^{rand} takes, it should ensure $\lambda_{PM} = 0$ in the PM regime more than T_G. In our case, we take T_c^{rand} as θ for $x = 0.1, 0.2$, which is now negative (positive) because of strong AFM (FM) coupling. For $x = 0.1$, the negative value of θ is considered to guarantee $\lambda_{PM} = 0$ above T_G. As a fitting result in the inset of Fig. 7, all λ_{GP} satisfy $0 \leqslant \lambda \leqslant 1$ in GP regions, further implying its GP behavior [30]. Based on the behavior of inverse susceptibility $\chi^{-1}(T)$, the higher value of λ represents the higher FM concentration and stronger contribution to the system due to a deviation from linear $\chi^{-1}(T)$ curves, while the lower λ stands for the lower FM interaction, which results in a PM state since a linear behavior appears in the plot of $\chi^{-1}(T)$. Accordingly, the λ_{GP} of $Sn_{0.8}NFe_{3.2}$ ($\lambda_{GP} = 0.57$) is higher than that of $Sn_{0.9}NFe_{3.1}$ ($\lambda_{GP} = 0.13$), indicating an enhanced FM interaction in $Sn_{0.8}NFe_{3.2}$, and this result agrees quite well with the analyses of magnetic properties. Now we begin to discuss the origin of the Griffith phase. In our system, we note that the GP appears in the fringe
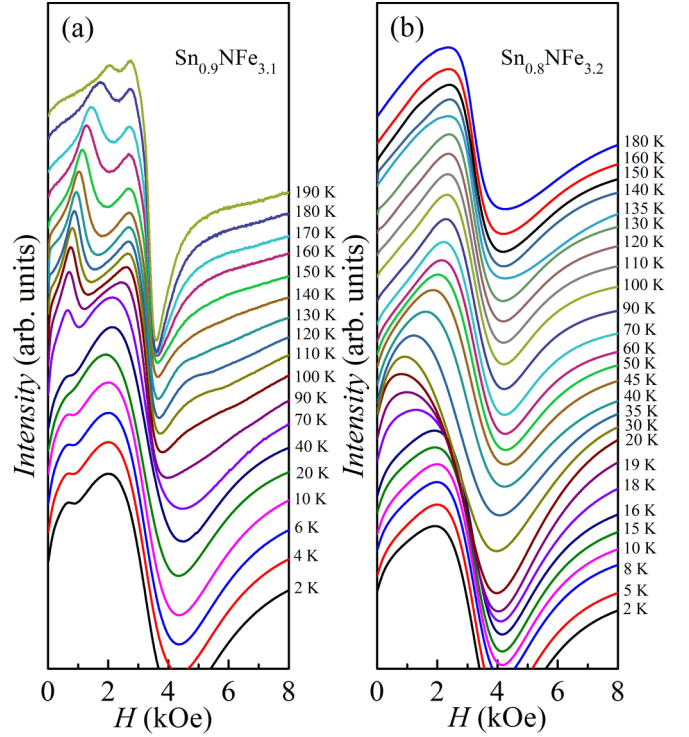
between FM interaction and AFM interaction. For $SnNFe_3$, AFM interaction dominates, with increasing Fe content, the iron-iron interactions are enhanced, and then the ferromagnetic cluster increases. It will lead to the competitions between AFM and FM interactions. With the further increase of iron content, the FM coupling will compete over the AFM one till FM interaction dominates. As a consequence, the present FM spin fluctuation in the PM state forms the short-range FM cluster below T_G [9], which is closely associated with the observed GP.

Since electron spin resonance (ESR) is helpful for directly understanding the magnetic interaction and spin correlation, we carried out the ESR measurements here. Figure 8 gives ESR derivative spectrums (dP/dH) for $Sn_{0.9}NFe_{3.1}$ and $Sn_{0.8}NFe_{3.2}$ with the temperature range from 2 to 190 K and 2 to 180 K, respectively. It should be pointed out that the FM phase transition can be identified by the defined expression $g = h\nu/\mu_B H_r$ (where h is the Plank constant, ν stands for the microwave frequency, μ_B represents the Bohr magnetor, and H_r stands for the resonance field) [31]. Especially, the g factor approaches 2 in the paramagnetic region calculated by the equation, and the corresponding resonance field H_r is about 3300 Oe. And according to the nominal definition, the FM signal is defined as the resonance field of absorption spectra is lower than that of the PM ($H_r < 3300$ Oe), while the AFM absorption peak is located at a higher H_r ($H_r > 3300$ Oe) [32]. As shown in Fig. 8(a), $Sn_{0.9}NFe_{3.1}$ exhibits several specific signals throughout the whole measurement temperature region, that is, the FM signal always exists in ESR spectrums even for $T > T_c^{rand}$ (or, equivalently, the temperature region
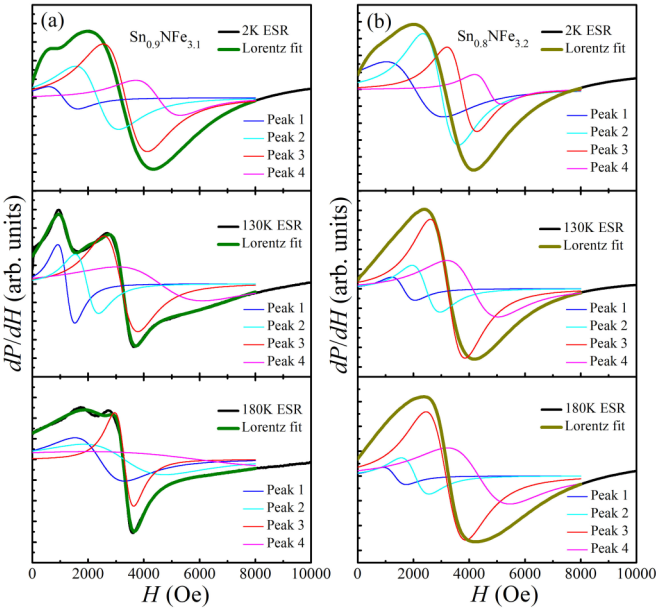
FIG. 9. The ESR spectra at some typical temperature fitted by Lorentzian lines: (a) for $Sn_{0.9}NFe_{3.1}$; (b) for $Sn_{0.8}NFe_{3.2}$. The individual curves represent the resolved components of the ESR spectra.

FIG. 10. Temperature dependent fitting parameters of ESR spectra H_r, g factor, and ΔH: (a) for $Sn_{0.9}NFe_{3.1}$; (b) for $Sn_{0.8}NFe_{3.2}$. Black shadow represents the GP temperature region, and yellow band is indexed as SG transition scale.

of PM state). This is the direct evidence for FM interaction in the system and is also well satisfied with the magnetization analyses discussed earlier. With increasing the doping concentration to $x = 0.2$, as seen in Fig. 8(b), $Sn_{0.8}NFe_{3.2}$ displays a much stronger FM signal at lower magnetic field, suggesting extensive FM interaction comparing to $x = 0.1$, which is in agreement with the descriptions in Fig. 7 since the GP is more prominent in $Sn_{0.9}NFe_{3.1}$ than in $Sn_{0.8}NFe_{3.2}$. In other words, a stronger FM interaction may make it easier to form long-range FM coupling rather than short-range FM correlation (i.e., GP).

Figure 9 shows the ESR spectrum lines for $Sn_{0.9}NFe_{3.1}$ and $Sn_{0.8}NFe_{3.2}$ respectively throughout the entire temperature range fitted by the Lorenzian profile [33]:

$$\frac{dP}{dH} \propto \frac{d}{dH}\left[\frac{\Delta H}{\Delta H^2 + (H - H_r)^2} + \frac{\Delta H}{\Delta H^2 + (H + H_r)^2}\right],$$
(1)

where P stands for the powder absorbed in the ESR measurement, H is the magnetic field, ΔH is the linewidth, and H_r represents the resonance field. As depicted clearly, the spectra can be well fitted by four Lorentzian-shape lines, and the results of specific peaks and fitted Lorentzian lines show that the micromagnetic structure is the coexistence of FM and AFM coupling [34], which are in good agreement with the GP studies and magnetization results. And here we focus on the fitting parameters of the sample $Sn_{0.9}NFe_{3.1}$ and $Sn_{0.8}NFe_{3.2}$. Figure 10 shows the H_r, g factor, and full width at half maximum (ΔH) plots as a function of temperature. As shown in the left panel of Fig. 10(a), there are four plot lines for each parameter, namely, P_1, P_2, P_3, and P_4. The peaks of signal around $H_r \sim 3300$ Oe with the g factor ~ 2 should be denoted as the PM signal, which is marked as P_3 in the plots. According to the expression aforementioned, P_1 and
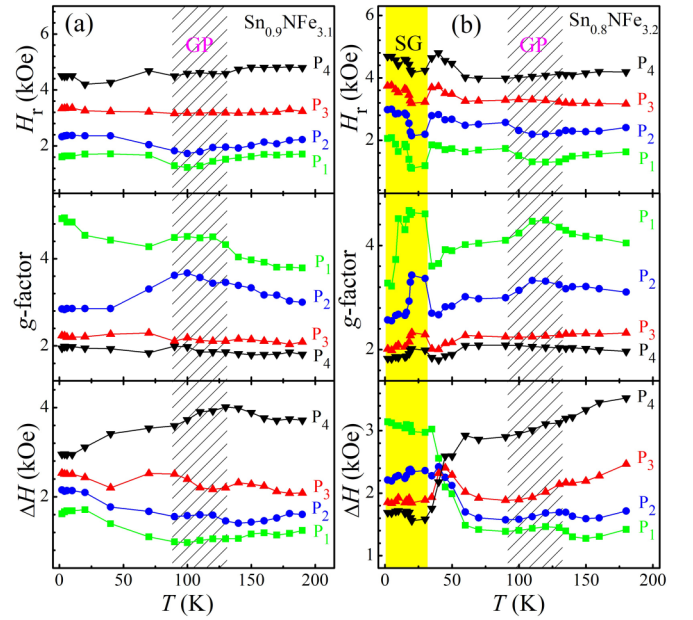
P_2 should be indexed as FM signals because of the lower H_r ($H_r < 3300$ Oe) and higher g factor ($g > 2$), arising from the Fe/Sn local FM cluster. Consequently, P_4 is identified as the AFM signal due to the much higher H_r ($H_r > 3300$ Oe) and lower g factor ($g < 2$) than that of PM, which is mainly caused by the Fe-N AFM interaction [12,22]. Similarly, Fig. 10(b) exhibits the same intrinsic feature for the plots of four fitting parameters, that is, P_1–P_4 stand for the specific magnetic signals, respectively. Differing from the $Sn_{0.9}NFe_{3.1}$, the SG phase is more prominent and marked with a yellow band for $Sn_{0.8}NFe_{3.2}$ below the T_f region. The GP regime pointed out both in Figs. 10(a) and 10(b) are almost distributed identically with the corresponding response to the varieties of fitting parameters. Obviously, the analysis results of ESR are well compatible with the above theoretical magnetic descriptions, implying the significant role of the short-range magnetic correlation, and confirming a transition to a slow dynamic regime, i.e., the GP state around $T_C(p) < T < T_G$ and SG behavior at lower temperature.

In our case, there are several magnetic interactions that exist in the system, and thus, we give the detailed magnetic phase diagram of $Sn_{1-x}NFe_{3+x}$ ($0 \leqslant x \leqslant 0.4$) to embody the dynamic magnetic transition as summarized in Fig. 11. For $x = 0$, the system behaves a magnetic fluctuation state, and the AFM interaction dominates. With increasing iron content x, the FM interaction is enhanced and AFM interaction is suppressed, and then, GP and SG behavior are observed as a matter of course. Outside of the Fe concentration threshold x_c with $0.1 \leqslant x_c \leqslant 0.2$, the GP disappears as well as exhibits a gradual decline of AFM interaction, and FM is dominant in the system subsequently. A MF state always exists in the system in the $0 \leqslant x \leqslant 0.4$ doping range, either resulting from the AFM-FM competitions or the short-range FM cluster, which
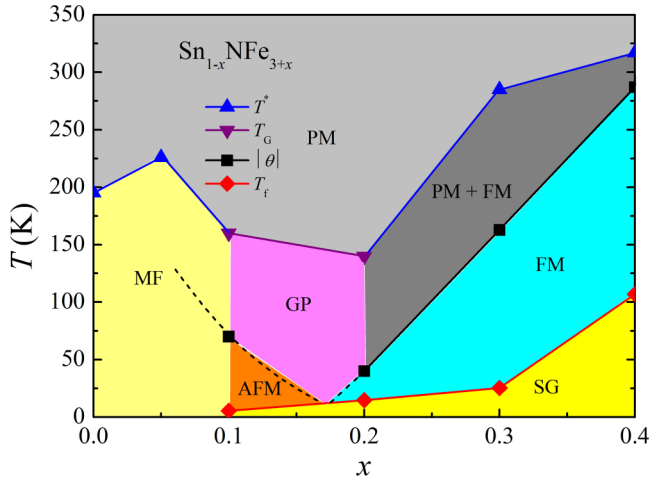
FIG. 11. The magnetic phase diagram incorporates several major dynamic transitions of $Sn_{1-x}NFe_{3+x}$ ($0 \leqslant x \leqslant 0.4$).

is consistent with the GP and SG behavior in the $Sn_{1-x}NFe_{3+x}$ series.

Nevertheless, we give sufficient characterizations and analyses for observed magnetic behavior; the theoretical calculation is necessary to support our investigations. As shown in Fig. 12(a), the summary DOS of $Sn_{0.7}NFe_{3.3}$ with specific s, p, and d states electrons are depicted based on the AFM state. It can be found that the d-state electrons contribution mainly locate around the Fermi level (E_f), while other s and p state electrons are distributed far away from the E_f, mainly devoting the spin distributions to weak sidebands. Differing from the AFM state, Fig. 12(b) gives the FM-state DOS with an unbalanced population with spin up and down. E_f locates at an upward slope of DOS curve, and shifts to lower energy. Moreover, the band structure of the crystal is computed along the high symmetry lines in the Brillouin zone as displayed in Fig. 12(c). For $Sn_{0.7}NFe_{3.3}$, an obvious spin-splitting occurs around the E_f, and the energy curve dispersion across the E_f

FIG. 12. (a) DOS for AFM $Sn_{0.7}NFe_{3.3}$. (b) DOS for polarized FM $Sn_{0.7}NFe_{3.3}$ under spin-up and -down states. (c) The GGA electronic band structure for $Sn_{0.7}NFe_{3.3}$. (d) The GGA electron distribution for $Sn_{0.7}NFe_{3.3}$ in the (-110) plane.

reflects the metallic behavior. The valence charge density of $Sn_{0.7}NFe_{3.3}$ is also performed in Fig. 12(d). In view of the reports of Segall et al. [35], the difference of valence charge density between two atoms in the overlap population serves as a criterion to identify the interactions, that is, the higher the value, the higher iconicity. Very clearly, many charges distribute at the intermediate region among the Fe and N atoms, immediately suggesting the characteristic of the strong hybridization for Fe-N; in other words, the Fe-N interactions are of covalent-ionic nature. However, the Sn-Fe bond ought to be metallic in nature since there is much less electron charge density locating between Sn and Fe, which means no significant interaction of them comparing with Fe-N. The results of bond analyses are very consistent with other similar cases of $PdFe_3N$ [36] and $NiFe_3N$ [37].

About the observed GP in the sample $Sn_{0.8}NFe_{3.2}$ and $Sn_{0.9}NFe_{3.1}$, we also performed the DFT calculations based on the spin-polarized FM and antiparallel spin AFM states in Fig. 13. For both $Sn_{0.8}NFe_{3.2}$ and $Sn_{0.9}NFe_{3.1}$, the bands near the Fermi level from -5 to 5 eV come mainly from the Fe 3 d-state electrons, and the intrinsic itinerant nature of the sample is embodied prominently since there is a large span of the Fe-3 d electrons [12]. An essential characteristic is the dissymmetry between spin-up and spin-down states for FM $Sn_{0.8}NFe_3$ as shown in Fig. 13(a). This differential distribution results in an increased net moment of DOS at E_f, reflecting the corresponding magnetic characteristic of $Sn_{0.8}NFe_3$. Figure 13(b) presents a nonpolarized net spin moment for $Sn_{0.9}NFe_{3.1}$ in a balanced DOS distribution. These theoretical calculations confirm our above analyses, that is, in low dopants $x \leqslant 0.1$, AFM interaction is dominant, while with increasing Fe doping concentration, the iron-iron interactions increase and thus lead to the increase of the FM cluster. As a result, it will lead to the competitions between AFM and FM interactions. Superimposing by the specific temperature, both the AFM-FM competitions under the T_f and the short-range FM cluster formed in the PM state below T_G should be responsible for the observed SG and GP.

In general, the appearance of SG is inextricably linked with the competitions between FM and AFM interactions which are the main cause of multiconfiguration of spins or spin frustrations. For example, in intermetallic URh_2Ge_2 [38] and $FeAl_2$ [39], the origin of SG behavior is attributed to the competitions between FM and AFM interactions. In our case, the AFM interaction is found in $Sn_{1-x}NFe_{3+x}$ ($0 \leqslant x \leqslant 0.1$), and the FM exchange is observed in the samples of $Sn_{1-x}NFe_{3+x}$ ($0.2 \leqslant x \leqslant 0.4$). Due to this system consisting of FM and AFM interactions, it can be understood that the SG behavior exists in $Sn_{0.7}NFe_{3.3}$ under the FM and AFM competitions. Similar to this case, both in Fe-based and Co-based antiperovskite compounds $SnCFe_3$ [22] and $GeNCo_3$ [40], SG behavior is proposed to originate from the atomic disorder introduced by the atomic deficiency, i.e., Sn and Ge deficiency for $SnCFe_3$ and $GeNCo_3$, respectively. Very recently, Zhang et al. [41] raised the nature of the SG of $Sn_xFe_{4-x}N$ through the neutron total scattering, from where, the SG is introduced by local FM cluster with a cluster size of ~ 8 Å on average. In consideration of these cases, we firmly believe that the disorder should occur since Sn occupies the corner position of the face-centered-cubic space structure, similar to
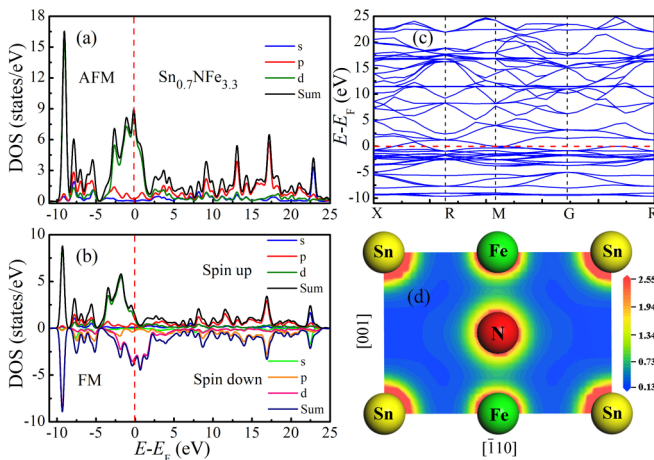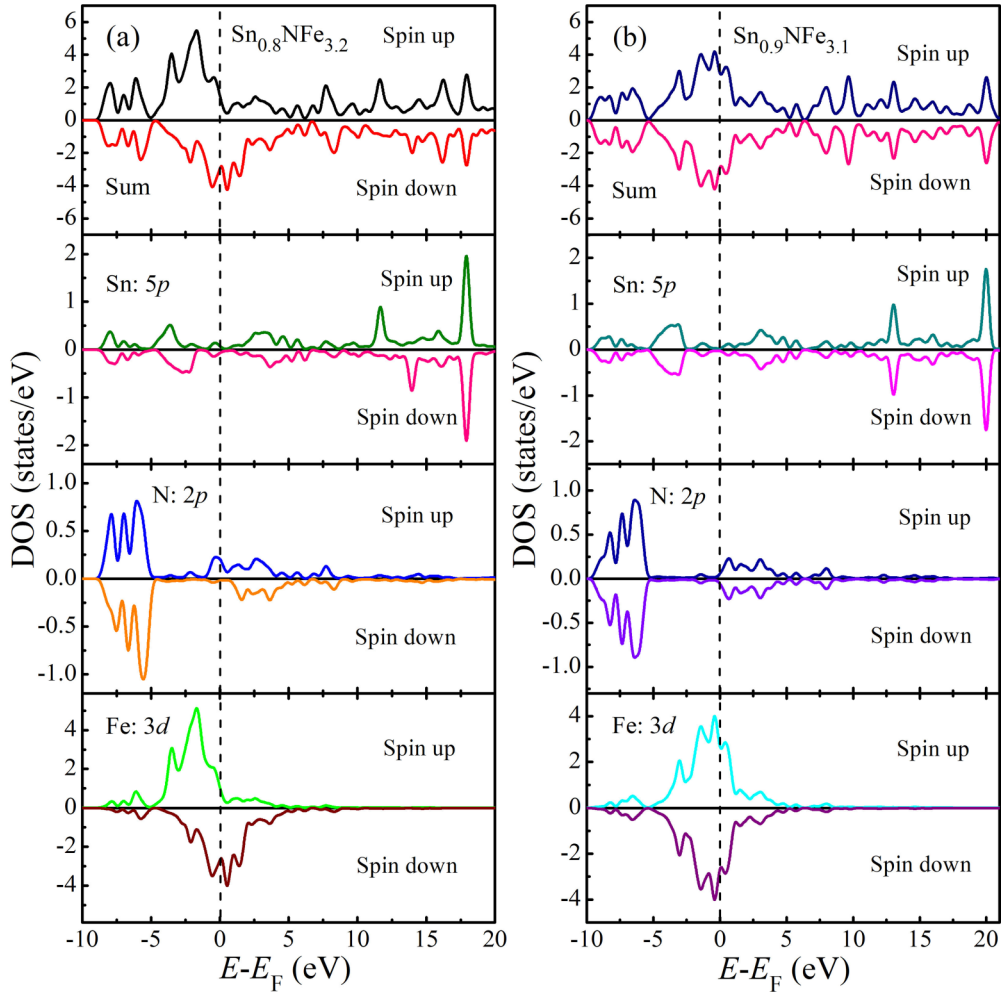
FIG. 13. The total and partial DOS of each atom for $Sn_{1-x}NFe_{3+x}$ ($x = 0.1, 0.2$): (a) for $x = 0.2$, $Sn_{0.8}NFe_{3.2}$; (b) for $x = 0.1$, $Sn_{0.9}NFe_{3.1}$.

$Sn_xFe_{4-x}N$, and forms the Fe/Sn local FM cluster. And thus, the SG behavior observed in $Sn_{1-x}NFe_{3+x}$ compounds may originate from the atomic disorder caused by a small amount of Sn deficiency, or the competitions between FM cluster and AFM interaction, or both [12].

Identifying the GP in limited dopants suggests the existence of Fe concentration threshold x_c with $0.1 \leqslant x_c \leqslant 0.2$. The fact that the GP is not observable outside this doping range confirms the intrinsic nature of the competitions of two magnetic interactions which results in FM spin fluctuation. The importance of the AFM and FM competition driven spin fluctuation and disorder has recently been reported to be crucial for the appearance of signatures of correlated clusters in the PM state [42]. Besides, inspired by the investigations of Ouyang *et al.* [9], for $Sn_{0.9}NFe_{3.1}$ and $Sn_{0.8}NFe_{3.2}$, no or less structural distortion exists, unlike the role of the Jahn-Teller (JT) effect for canonical Mn-based perovskite compounds, which causes the JT distorted orthorhombic to rhombohedral phase [28]. That is, as the random distribution of the FM bond starts to fluctuate along with the fluctuating lattice distortion, indicating the source of a GP in our compound is somewhat different from JT structural distortion, which the symmetric superexchange can be constructed using an Ising

spin chain with nearest-neighbor FM (J_{FM}) and next-nearest-neighbor AFM (J_{AFM}) competing interactions [43]. However, the intrinsic magnetic ground has been revealed by neutron-diffraction studies that the local FM cluster is identified for $Sn_{0.88}Fe_{3.12}N$ in the frustration and disorder state and well maintained [41]. The above result gives a reliable evidence revealing the existence of local FM correlation in our system, and such correlation length should benefit the theoretical description for the GP system.

IV. CONCLUSIONS

In summary, we have experimentally identified an entire GP in antiperovskite Fe-based nitrides $Sn_{1-x}NFe_{3+x}$ ($0 \leqslant x \leqslant 0.4$). Through the systemic magnetic measurements, as the x level increases, magnetic interaction changes from MF behavior at $x = 0$ to AFM interaction at $x = 0.05$ and 0.1, and then to FM interaction at $0.2 \leqslant x \leqslant 0.4$. Along with this process, the FM spin fluctuation in the PM state forms the short-range FM cluster, which leads to the appearance of the GP at $x = 0.1$ and 0.2. This phase regime arises as a result of the strong atomic disorder by diluting the element substitution for Fe sites, and thus, the enhanced GP is observed for $Sn_{0.9}NFe_{3.1}$

comparing with $Sn_{0.8}NFe_{3.2}$. In addition, a canonical SG behavior is found at low temperature in $Sn_{0.7}NFe_{3.3}$, which can be attributed to the competitions between FM and AFM interactions. The DFT calculations confirm the specific magnetic coupling and atomic interaction in $Sn_{1-x}NFe_{3+x}$ series which incorporate the FM-AFM competitions and atomic disorder in the system.

[1] R. B. Griffiths, Phys. Rev. Lett. **23**, 17 (1969).

[2] D. Akahoshi, M. Uchida, Y. Tomioka, T. Arima, Y. Matsui, and Y. Tokura, Phys. Rev. Lett. **90**, 177203 (2003).

[3] W. Jiang, X. Z. Zhou, and G. Williams, Y. Mukovskii, and K. Glazyrin, Phys. Rev. B **76**, 092404 (2007).

[4] M. Hennion, F. Moussa, G. Biotteau, J. Rodriguez-Carvajal, L. Pinsard, and A. Revcolevschi, Phys. Rev. Lett. **81**, 1957 (1998).

[5] J. M. D. Teresa, M. R. Ibarra, P. A. Algarabel, C. Ritter, C. Marquina, J. Blasco, J. García, A. del Moral, and Z. Arnold, Nature (London) **386**, 256 (1997).

[6] H. Deguchi, M. Aikawa, K. Ohtani, and S. Takagi, J. Magn. Magn. Mater. **177-181**, 87 (1998).

[7] S. Guo, D. P. Young, R. T. Macaluso, D. A. Browne, N. L. Henderson, J. Y. Chan, L. L. Henry, and J. F. DiTusa, Phys. Rev. Lett. **100**, 017209 (2008).

[8] V. Y. Pomjakushin, D. V. Sheptyakov, K. Conder, E. V. Pomjakushina, and A. M. Balagurov, Phys. Rev. B **75**, 054410 (2007).

[9] Z. W. Ouyang, N. M. Xia, Y. Y. Wu, S. S. Sheng, J. Chen, Z. C. Xia, and L. Li, and G. H. Rao, Phys. Rev. B **84**, 054435 (2011).

[10] C. Magen, P. A. Algarabel, L. Morellon, J. P. Araújo, C. Ritter, M. R. Ibarra, A. M. Pereira, and J. B. Sousa, Phys. Rev. Lett. **96**, 167201 (2006).

[11] K. Ghosh, C. Mazumdar, R. Ranganathan, and S. Mukherjee, Sci. Rep. **5**, 15801 (2015).

[12] C. C. Liu, X. Y. N. Tao, X. C. Kan, X. S. Liu, C. H. Zhang, S. J. Feng, Y. J. Yang, Q. R. Lv, J. Y. Hu, and M. Shezad, Appl. Phys. Lett. **116**, 052401 (2020).

[13] S. J. Clark, M. D. Segall, C. J. Pickard, P. J. Hasnip, M. I. J. Probert, K. Refson, and M. C. Payne, Z. Kristallogr. **220**, 567 (2005).

[14] W. Kohn and L. J. Sham, Phys. Rev. **140**, A1133 (1965).

[15] J. P. Perdew, K. Burke, and M. Ernzerhof, Phys. Rev. Lett. **77**, 3865 (1996).

[16] T. Scholz and R. Dronskowski, Inorg. Chem. **54**, 8800 (2005).

[17] X. C. Kan, B. S. Wang, S. Lin, B. Yuan, L. Zu, X. F. Wang, J. C. Lin, P. Tong, W. H. Song, and Y. P. Sun, J. Alloy Compd. **663**, 94 (2016).

[18] W. J. Feng, D. Li, W. J. Ren, Y. B. Li, W. F. Li, J. Li, Y. Q. Zhang, and Z. D. Zhang, Phys. Rev. B **73**, 205105 (2006).

[19] L. Zu, S. Lin, Y. Liu, J. C. Lin, B. Yuan, X. C. Kan, P. Tong, W. H. Song, and Y. P. Sun, Appl. Phys. Lett. **108**, 031906 (2016).

[20] X. C. Kan, B. S. Wang, L. Zhang, L. Zu, S. Lin, J. C. Lin, P. Tong, W. H. Song, and Y. P. Sun, Phys. Chem. Chem. Phys. **19**, 13703 (2017).

[21] X. H. Zhang, Q. Yuan, J. C. Han, J. G. Zhao, J. K. Jian, Z. H. Zhang, and B. Song, Appl. Phys. Lett. **103**, 022405 (2013).

[22] B. S. Wang, P. Tong, Y. P. Sun, X. B. Zhu, Z. R. Yang, W. H. Song, and J. M. Dai, Appl. Phys. Lett. **97**, 042508 (2010).

[23] J. C. Lin, P. Tong, D. P. Cui, C. Yang, S. Lin, W. J. Lu, B. S. Wang, B. C. Zhao, and Y. P. Sun, Phys. Status Solidi B **252**, 582 (2015).

[24] S. Lin, D. F. Shao, J. C. Lin, L. Zu, X. C. Kan, B. S. Wang, Y. N. Huang, W. H. Song, W. J. Lu, P. Tong, and Y. P. Sun, J. Mater. Chem. C **3**, 5683 (2015).

[25] J. A. Mydosh, *Spin Glasses: An Experimental Introduction* (Taylor & Francis, London, 1993).

[26] A. Aharoni and E. P. Wohlfarth, J. Appl. Phys. **55**, 1664 (1984).

[27] R. F. Yang, Y. Sun, W. He, Q. A. Li, and Z. H. Cheng, Appl. Phys. Lett. **90**, 032502 (2007).

[28] J. Deisenhofer, D. Braak, H. A. Krug von Nidda, J. Hemberger, R. M. Eremina, V. A. Ivanshin, A. M. Balbashov, G. Jug, A. Loidl, T. Kimura, and Y. Tokura, Phys. Rev. Lett. **95**, 257202 (2005).

[29] W. J. Jiang, X. Z. Zhou, and G. Williams, Europhys. Lett. **84**, 47009 (2008).

[30] A. H. Castro Neto, G. Castilla, and B. A. Jones, Phys. Rev. Lett. **81**, 3531 (1998).

[31] C. Rettori, D. Rao, J. Singley, D. Kidwell, S. B. Oseroff, M. T. Causa, J. J. Neumeier, K. J. McClellan, S. W. Cheong, and S. Schultz, Phys. Rev. B **55**, 3083 (1997).

[32] Z. W. Ouyang, H. Nojiri, S. Yoshii, G. H. Rao, and Y. C. Wang, Phys. Rev. B **80**, 054401 (2009).

[33] S. Uma, T. Vasilchikova, A. Sobolev, G. Raganyan, A. Sethi, H. J. Koo, M. H. Whangbo, I. Presniakov, I. Glazkova, A. Vasiliev, S. Streltsov, and E. Zvereva, Inorg. Chem. **58**, 11333 (2019).

[34] J. Yang, W. Tong, Z. Liu, X. B. Zhu, J. M. Dai, W. H. Song, Z. R. Yang, and Y. P. Sun, Phys. Rev. B **86**, 104410 (2012).

[35] M. D. Segall, R. Shah, C. J. Pickard, and M. C. Payne, Phys. Rev. B **54**, 16317 (1996).

[36] P. Mohn, K. Schwarz, S. Matar, and G. Demazeau, Phys. Rev. B **45**, 4000 (1992).

[37] D. Music and J. M. Schneider, Appl. Phys. Lett. **88**, 031914 (2006).

[38] S. Süllow, G. J. Nieuwenhuys, A. A. Menovsky, J. A. Mydosh, S. A. M. Mentink, T. E. Mason, and W. J. L. Buyers, Phys. Rev. Lett. **78**, 354 (1997).

[39] C. S. Lue, Y. Öner, D. G. Naugle, and J. H. Ross, Phys. Rev. B **63**, 184405 (2001).

[40] L. Zu, S. Lin, J. C. Lin, B. Yuan, X. C. Kan, P. Tong, W. H. Song, and Y. P. Sun, Inorg. Chem. **55**, 9346 (2016).

[41] Y. P. Zhang, T. Scholz, R. Dronskowski, M. T. McDonnell, and M. G. Tucker, Phys. Rev. B **100**, 014419 (2019).

[42] V. Kiryukhin, New J. Phys. **6**, 155 (2004).

[43] Y. J. Choi, H. T. Yi, S. Lee, Q. Huang, V. Kiryukhin, and S. W. Cheong, Phys. Rev. Lett. **100**, 047601 (2008).